



# Catalytic pyrolysis of fatty acids and oils into liquid biofuels and chemicals over supported Ni catalysts on biomass-derived carbon

Bin Chen<sup>a</sup>, Zining Zhou<sup>b</sup>, Yuze Li<sup>a</sup>, Kok Bing Tan<sup>b</sup>, Youting Wang<sup>b</sup>, Xiaoping Rao<sup>b</sup>,  
Jiale Huang<sup>a,\*</sup>, Xiaodong Zhang<sup>c</sup>, Qingbiao Li<sup>a,c</sup>, Guowu Zhan<sup>b,\*</sup>

<sup>a</sup> College of Chemistry and Chemical Engineering, Xiamen University, 422 Siming South Road, Xiamen 361005, Fujian, China

<sup>b</sup> College of Chemical Engineering, Integrated Nanocatalysts Institute (INCI), Academy of Advanced Carbon Conversion Technology, Huaqiao University, 668 Jimei Avenue, Xiamen 361021, Fujian, China

<sup>c</sup> College of Marine Equipment and Mechanical Engineering, Jimei University, 185 Ynjiang Road, Xiamen 361021, Fujian, China

## ARTICLE INFO

### Keywords:

Biomass-derived carbon  
Fatty acids  
Oils  
Catalytic pyrolysis  
H<sub>2</sub>-free

## ABSTRACT

Herein, biomass-derived activated carbon (bio-AC) was synthesized using rice husk as a biotemplate and natural carbon source. After immobilization of Ni, the supported Ni/bio-AC showed excellent catalytic activity in the pyrolysis of fatty acids to paraffin-based biodiesel in H<sub>2</sub>-free and solvent-free conditions, corresponding to the conversion of 99.6% and a total alkane yield of 95.1%, including 88.9% heptadecane. Based on comprehensive characterizations, the calculated turnover frequency of Ni/bio-AC was 3.9 times that of conventional Ni/AC. Significantly enhanced olefin selectivity was further obtained by N-doping of Ni/bio-AC, which was attributed to the inhibition of -COO\* dissociation by the Ni-N sites. The possible catalytic reaction pathways from stearic acid to heptadecane via aliphatic alcohol as a reaction intermediate were investigated. Besides, efficient conversions of saturated and unsaturated plant oils were also achieved over Ni/bio-NAC catalysts in Py-GC/MS through pulsed catalytic pyrolysis manner, showing a promising prospect for sustainable biofuels and chemical production.

## 1. Introduction

The growing greenhouse effect and the huge energy supply gap have stimulated the development of biomass-related energy as an alternative source to traditional non-renewable fossil fuels [1–3]. For instance, natural lipids composed of triglycerides are important bio-feedstocks for the production of liquid biofuels and high-value chemicals through catalytic pyrolysis due to their high energy density and scalability [4–8]. The catalytic pyrolysis process generally involves complex reactions such as deoxygenation, isomerization, and aromatization [9,10]. Catalytic deoxygenation of lipids is the key to improving the quality and stability of the pyrolysis products, as high oxygen content can lead to the low calorific value, high viscosity, and deterioration [11]. Fatty acids occupy about 95% of the molecular mass of triglycerides and are often used as model compounds for catalytic deoxygenation reactions of lipids. Hydrodeoxygenation, decarboxylation, and decarbonylation are the three main pathways for the catalytic deoxygenation of fatty acids

[12–14].

Much research has been devoted to developing high-performing deoxygenation catalysts in recent years and significant progress has been made. For example, a series of metal catalysts supported on carbon [15,16], TiO<sub>2</sub> [17], SiO<sub>2</sub> [18,19], ZrO<sub>2</sub> [14], and Al<sub>2</sub>O<sub>3</sub> [20] materials have been developed for the deoxygenation of fatty acids. Among these, noble metal catalysts with unfilled *d*-orbital electron configurations exhibit excellent catalytic performance. For instance, the Pd/C catalyst was able to achieve efficient hydrodeoxygenation of stearic acid with *n*-alkane yields up to 96.0% after 30 min of reaction [19]. It was also found that the type of catalyst support had a dominant effect on the hydrodeoxygenation performance of stearic acid, with the initial decarboxylation rate over Pd/C ( $202 \times 10^3 \text{ s}^{-1}$ ) significantly higher than that over Pd/SiO<sub>2</sub> ( $34 \times 10^3 \text{ s}^{-1}$ ) or Pd/Al<sub>2</sub>O<sub>3</sub> ( $27 \times 10^3 \text{ s}^{-1}$ ). The reason might be possibly due to the strong adsorption capacity of the carbon material for fatty acids [18]. In addition, other noble metal catalysts (e. g., Pt [21,22], Ru [17,23], Rh [16], etc.) loaded on carbon support also

\* Corresponding authors.

E-mail addresses: [cola@xmu.edu.cn](mailto:cola@xmu.edu.cn) (J. Huang), [gwzhan@hqu.edu.cn](mailto:gwzhan@hqu.edu.cn) (G. Zhan).

<sup>1</sup> 0000-0001-9069-5739

<sup>2</sup> 0000-0002-6337-3758

<https://doi.org/10.1016/j.apcatb.2023.123067>

Received 21 April 2023; Received in revised form 30 June 2023; Accepted 2 July 2023

Available online 3 July 2023

0926-3373/© 2023 Elsevier B.V. All rights reserved.

exhibited good catalytic performance in the hydrodeoxygenation of fatty acids to diesel-range alkanes. For the Pd and Pt catalysts, the fatty acids underwent catalytic deoxygenation mainly via the decarboxylation and decarbonylation pathways, while hydrodeoxygenation tended to occur on the Ru catalysts [9].

Recently, some researchers have introduced other transition metals into noble catalysts to further enhance the deoxygenation activity and modulate the product selectivity [13,24]. For instance, Janampelli et al. found that the introduction of Mo or W in Pt/ZrO<sub>2</sub> would significantly enhance the deoxygenation activity of oleic acid and improve octadecane selectivity [12]. Furthermore, the introduction of the second type of metal can also effectively alter the reaction pathway and promote the formation of thermodynamically unfavorable products, such as long-chain alkenes. Recently, a metal-organic framework-derived PtZn/C catalyst was fabricated for selective deoxygenation of lauric acid to undecene in H<sub>2</sub>-free condition with a selectivity of 67%, much higher than that of Pt/C (27.5%) and Zn/C (10.6%) [25]. This is attributed to the interaction of Pt with Zn, which inhibits the decarboxylation pathway and reduces the desorption energy of CO.

Nevertheless, the high cost and ease of deactivation are two main obstacles to the application of noble metal catalysts. Therefore, cheap transition metal catalysts (Ni [26–28], Co [29], Cu [30,31], Mn [32], and W [15,33], etc.) were also developed, among which Ni-based metal catalysts were found to possess good performance with similar deoxygenation activity as noble metals [9]. For instance, Yang et al. prepared Ni/ZrO<sub>2</sub> catalysts by urea precipitation method and achieved efficient hydrodeoxygenation of methyl laurate with the conversion of 100% and the yield of alkanes of 99.4% [28]. Cao et al. found that NiRe bimetallic catalyst supported on SBA-15 exhibited excellent hydrodeoxygenation performance towards stearic acid with an alkane yield of 95.0%, which was significantly better than Ni, NiMo, NiFe, and NiCu catalysts [34]. The reason can be attributed to the improved dispersion and hydrogen activation of metal Ni after the introduction of Re and promoted the adsorption of reaction substrate and intermediates.

Excellent progress has been made in the production of liquid biofuels (alkane products) by hydrodeoxygenation of fatty acids and oils, but the use of high-pressure hydrogen suffers from high costs and safety risks that limit its large-scale application [35]. Accordingly, some researchers have attempted to catalyze fatty acid deoxygenation in H<sub>2</sub>-free and solvent-free systems in recent years, particularly, using Ni-based and Pd-based metal catalysts [36,37]. For instance, the NiFe@C catalyst showed excellent performance in the H<sub>2</sub>-free and solvent-free deoxygenation of stearic acid with a conversion of 99.9% and a heptadecane selectivity of 76.8% [27]. However, the expensive Pd/ $\gamma$ -Al<sub>2</sub>O<sub>3</sub> catalyst gave only 10.0% catalytic conversion of stearic acid and 79.0% selectivity for heptadecane under H<sub>2</sub>-free and solvent-free conditions [36]. The decreasing cyclic catalytic performance of Ru/C and NiFe/SiO<sub>2</sub> catalysts for H<sub>2</sub>-free deoxygenation of fatty acids has been reported in the literature [16,27,38]. Furthermore, based on the thermodynamic parameters of fatty acid deoxygenation at 573 K, the process of decarboxylation of fatty acids to alkanes ( $\Delta G_{573} = -83.5$  kJ/mol,  $\Delta H_{573} = 9.2$  kJ/mol) is more favorable than that of decarbonylation of fatty acids to olefins ( $\Delta G_{573} = -17.0$  kJ/mol,  $\Delta H_{573} = 179.1$  kJ/mol) [39]. As a result, in the vast majority of research, the selectivity for long-chain olefin products is commonly poor [40].

In this work, rice husk (RH), which is rich in organic carbon and possesses a natural pore structure, was selected as the biotemplate and carbon source for the preparation of biomass-derived activated carbon (bio-AC). The biotemplate-derived porous materials would inherit highly ordered multi-level skeletal structures and abundant surface functional groups (e.g., oxygen-containing and nitrogen-containing groups, etc.) [41–43]. Subsequently, the supported Ni/AC and Ni/bio-AC catalysts were obtained by loading Ni onto commercial activated carbon (AC) and bio-AC using an adsorption reduction method. The catalytic performance of bio-AC, Ni/bio-AC, and Ni/AC catalysts was evaluated and compared for catalytic deoxygenation of

fatty acids under H<sub>2</sub>-free and solvent-free conditions. The possible catalytic reaction pathways from stearic acid to heptadecane over Ni/bio-AC catalysts were investigated. In addition, N elements were doped into Ni/bio-AC (termed Ni/bio-NAC) to regulate the distribution of deoxygenation products, and the corresponding regulatory mechanisms were explored. Furthermore, the H<sub>2</sub>-free pulsed catalytic pyrolysis performance of Ni/bio-NAC for fatty acids and oils with different properties was evaluated by an analytical pyrolysis-gas chromatography/mass spectrometry (Py-GC/MS).

## 2. Experimental section

### 2.1. Materials

The following chemicals were used without further purification. Potassium hydroxide (90%, Adamas), nickel (II) nitrate hexahydrate (Ni(NO<sub>3</sub>)<sub>2</sub>·6 H<sub>2</sub>O, 99%, Adamas), melamine (99%, Adamas), stearic acid (99.5%, Aladdin), heptadecane (C<sub>17</sub>, 99%, Aladdin), 1-heptadecene (C<sub>17</sub>, 99.5%, Aladdin), 1-octadecanol (C<sub>18</sub>OH, 98%, Aladdin), octadecane (C<sub>18</sub>, 99%, Aladdin), hexadecane (99%, Aladdin), pentadecane (99%, Aladdin), tetradecane (99%, Aladdin), palmitic acid (99%, Aladdin), tetradecanoic acid (99%, Aladdin), lauric acid (99%, Aladdin), oleic acid (99%, Aladdin), linoleic acid (99%, Aladdin). Distilled water and anhydrous ethanol (99.99%) were used for all experiments. The RH was purchased from a farmer in Xiamen, Fujian Province, China. The commercial granular activated carbon (AC) was purchased from Sino-pharm Group Co., Ltd.

### 2.2. Fabrication method of catalyst materials

#### 2.2.1. Synthesis of bio-AC

The raw RH material was first crushed and sieved to obtain a powdery sample with a mesh size of 60. Subsequently, the RH powder was calcined at 500 °C under N<sub>2</sub> atmosphere for 1 h. Next, the carbonized black powder was ground with potassium hydroxide (mass ratio of 1:3) until homogeneous and calcined at 750 °C under N<sub>2</sub> atmosphere for 1 h. Finally, the obtained bio-AC was washed several times with deionized water.

#### 2.2.2. Synthesis of Ni/bio-AC and Ni/AC

0.3 g of bio-AC (as support material) was dispersed in 10 mL of aqueous nickel nitrate solution (17.9 mM) by sonication. After stirring vigorously for 4 h at room temperature, solid samples were collected by centrifugation. Subsequently, the dried samples were reduced for 2 h at 600 °C under 5% H<sub>2</sub>/Ar atmosphere. Similarly, for the preparation of Ni/AC, the bio-AC carrier was replaced with commercial AC and the other preparation procedures were identical.

#### 2.2.3. Synthesis of bio-NAC and Ni/bio-NAC

Bio-NAC was prepared in the same way as bio-AC, except that an additional amount of melamine was added during the grinding process with potassium hydroxide. Subsequently, the Ni/bio-NAC was prepared in the same way as Ni/bio-AC, except that the bio-AC carrier was replaced with bio-NAC.

### 2.3. Catalyst performance evaluation method

Batch catalytic deoxygenation of stearic acid was performed in a micro-batch reactor (volume: 1.67 mL, Swagelok, USA). For a typical evaluation, the sealed reactor containing 60 mg of stearic acid and 18 mg of catalyst was heated at 360 °C for 0.5 h, giving a mass ratio of substrate to catalyst of 3.33. After the reaction was completed, the reactor was cooled in cold water to terminate the reaction. Qualitative analysis of the products was carried out on a Thermo ISQ7000 instrument with a TS-1 ms capillary column (GC/MS). The products were quantified using gas chromatography (GC, Agilent 7890 A) equipped

with a flame ion detector (FID) and an Agilent CP-FFAP CB capillary column ( $30\text{ m} \times 0.32\text{ mm} \times 0.33\text{ }\mu\text{m}$ ). The correction factors for the reactants and products were calculated using the corresponding standard samples and then were used to calculate the conversion and selectivity data. Furthermore, the catalytic pyrolysis performance of various fatty acids and oils under flow conditions was evaluated by an analytical pyrolysis-gas chromatography/mass spectrometry (Py-GC/MS, Agilent CDS 5200–7890 A/5975 C). For a typical evaluation, the amount of fatty acid dosed was 0.5 mg per dose, 5 mg of catalyst was loaded into a quartz reactor, and pure  $\text{N}_2$  was used as the carrier gas at a flow rate of 101.2 mL/min.

#### 2.4. Characterization methods

The surface morphology and fine structure of the catalysts were analyzed by scanning electron microscope (SEM, Zeiss Sigma) and scanning transmission electron microscope (STEM, FEI Talos F200x). The elemental composition and distribution of the samples were detected by X-ray energy dispersive spectroscopy (EDX) on the STEM equipped with the corresponding accessory. X-ray photoelectron spectroscopy (XPS, AXIS-HSi, Kratos Analytical) was used to analyze the surface composition and metal valence of the catalysts. To minimize interference with elemental carbon analysis, the sample was attached to the holder using ordinary double-face adhesive tape rather than carbon conductive tape and then placed on an insulating ceramic carousel [44]. The chemical composition of the raw rice husk was determined by X-ray fluorescence spectroscopy (XRF) (ARL Perform X 4200, ThermoFisher Scientific). The  $^{13}\text{C}$  MAS NMR spectra of catalysts were examined by a Bruker 400 M (Agilent) instrument (10 kHz). The  $\text{N}_2$  adsorption-desorption isotherms, DFT (Density Functional Theory) pore size distributions, and specific BET (Brunauer-Emmett-Teller) surface area were examined on a Quantachrome (Autosorb-iQ-2MP). The X-ray

diffraction (XRD) patterns of the samples were recorded on a Rigaku Ultima IV operated at 40 kV and 30 mA employing  $\text{Cu K}\alpha$  radiation ( $\lambda = 1.54\text{ }\text{\AA}$ ). Fourier transform infrared (FT-IR) absorption spectra of the samples were recorded on a Nicolet 6700. The metal content of catalysts was conducted by inductively coupled plasma-optical emission spectrometry (ICP-OES) on Agilent 5110. The Raman spectra were examined by a spectrometer (Renishaw, InVia) employing a 532 nm laser as the excitation source. The strength of acid sites on catalysts was probed by ammonia temperature programmed desorption ( $\text{NH}_3$ -TPD) on a Micromeritics AutoChem II 2920. The nature of acid sites on catalysts was characterized via pyridine-adsorbed FTIR (Py-FTIR) analysis on a Nicolet 6700.

In-situ diffuse reflectance infrared Fourier transform spectra (in-situ DRIFTS) were obtained on a Nicolet iS-50 spectrometer equipped with a mercury-cadmium-tellurium (MCT) detector and a KBr optical beam splitter operated at a resolution of  $4\text{ cm}^{-1}$  and a wavenumber range from 4000 to  $650\text{ cm}^{-1}$ . The fatty acids and catalyst (mass ratio of 3.33) were placed in a reaction chamber (Harrick) with temperature-controlled equipment and ZnSe windows for online detection of changes in functional groups and gaseous products at different temperatures.

### 3. Results and discussion

#### 3.1. Characterization and catalytic activity of bio-AC

As displayed in Fig. 1a, the RH-derived activated carbon (bio-AC) was synthesized by two steps: (i) carbonization of RH under an  $\text{N}_2$  atmosphere; (ii) high-temperature etching of the carbonized RH with potassium hydroxide (i.e., activation) to obtain a rich pore structure. The SEM images showed that bio-AC inherited the hierarchical structure and porosity of RH (Fig. 1b–d). In contrast, the commercial AC exhibited an aggregated bulk structure (Fig. 1e). The XRD pattern of bio-AC

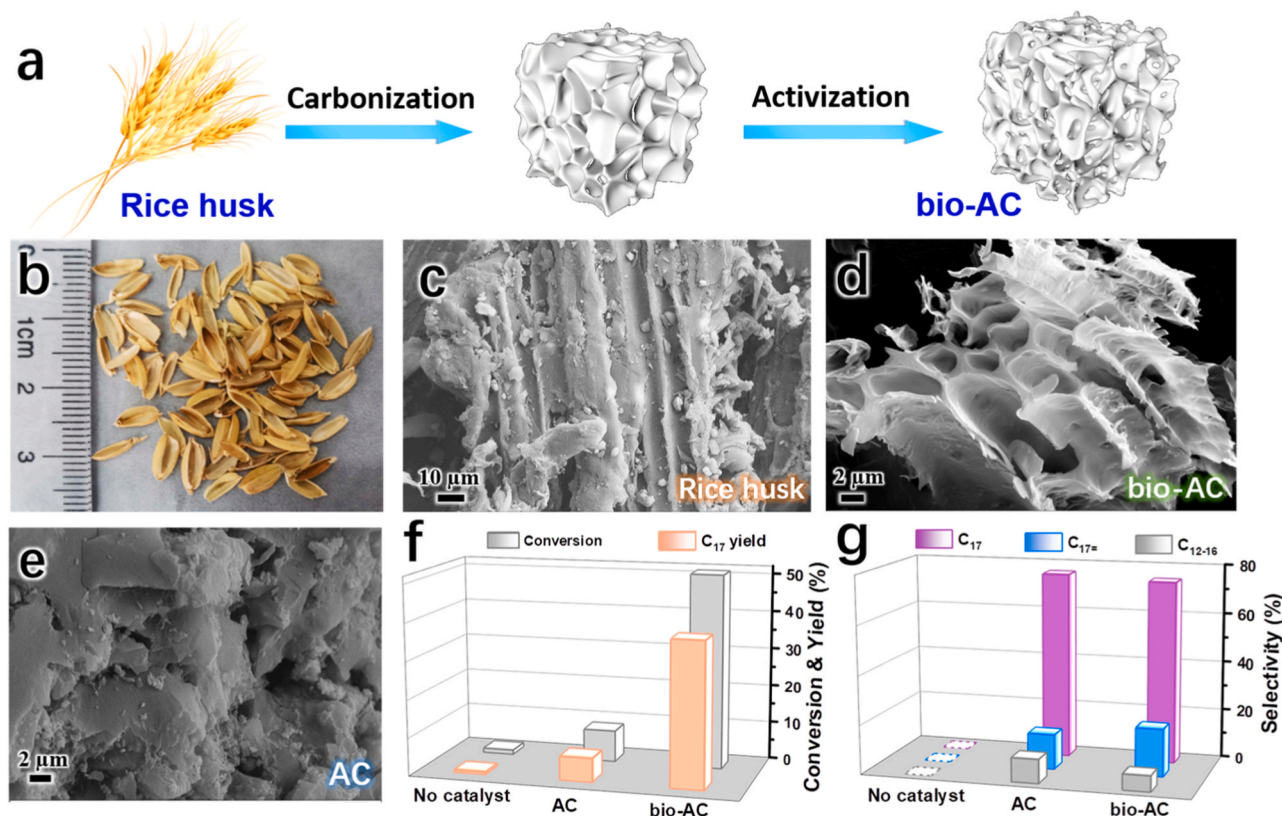


**Fig. 1.** (a) Schematic illustration of the preparation of bio-AC from RH, (b) digital photograph of the raw RH, SEM images of (c) RH, (d) bio-AC, and (e) AC, (f) catalytic performance of AC and bio-AC in the  $\text{H}_2$ -free catalytic deoxygenation of stearic acid in a micro-batch reactor, and (g) the corresponding product distribution in different examples.



exhibited two broad peaks at  $2\theta \approx 22^\circ$  and  $44^\circ$ , demonstrating the formation of active carbon with low crystallinity (Fig. S1). Next, the catalytic activities of both bio-AC and AC were evaluated towards  $H_2$ -free catalytic deoxygenation of lipids in a micro-batch reactor (using stearic acid as a model compound). As can be seen in Fig. 1f, g, the stearic acid was hardly converted in the absence of the catalyst. Surprisingly, the conversion of stearic acid over AC was 8.3%, while bio-AC showed a remarkably enhanced conversion of 51.2%. In both cases, the product distribution was similar, that is, heptadecane ( $C_{17}$ ) was the major product ( $\sim 75\%$ ), and a small amount of heptadecene ( $C_{17}$ ,  $\sim 16.5\%$ ) and short-chain alkanes ( $C_{12}$ – $C_{16}$ ,  $\sim 8.5\%$ ) were found in the product.

To probe the intrinsic catalytically active sites of the carbonaceous materials (bio-AC and AC), the surface atomic composition of AC and bio-AC was analyzed using XPS. The survey scan spectra reveal that both carbonaceous supports were rich in oxygen species (Fig. 2a), wherein, the surface oxygen content was 11.2% and 10.1%, respectively, for bio-AC and AC samples (Fig. S2). Furthermore, the XPS spectra in the C 1 s region revealed that the oxygen-containing groups were mainly C=O and C-O-C/C-OH (Fig. 2b). Compared to AC, bio-AC possessed a higher amount of C-O-C/C-OH groups (12.1 vs. 9.6%). A similar result was also found in the XPS spectra in the O 1 s region, confirming the abundant oxygen-containing groups (Fig. S3). The  $^{13}C$  MAS NMR spectra revealed that the  $sp^2$  carbon nucleus of bio-AC was located at a lower field position (117 vs. 125  $cm^{-1}$ ) compared to that of AC (Fig. 2c). This indicated that the aromatic carbon of bio-AC possessed more oxygen-containing groups with induced effects [45,46], which was consistent with the XPS results.

By  $H_2$  treatment, the amount of these oxygen-containing groups would be reduced as confirmed by FTIR spectra (Fig. S4). Interestingly, catalytic performance evaluation results revealed that  $H_2$ -treated bio-AC had led to a decrease in deoxygenation activity towards stearic acid (Fig. 2d), indicating that oxygen-containing groups had catalytic activity for fatty acid deoxygenation. This is consistent with the previous works that oxygen-containing groups (e.g., COOH and C-OH) possess intrinsic catalytic activity for some reaction processes (e.g.,  $CO_2$  reduction reaction or oxygen reduction reaction) [47,48]. In addition,  $N_2$  physisorption characterization reveals that bio-AC has a much higher

specific BET surface area ( $S_{BET}$ , 2670 vs. 879  $m^2 g^{-1}$ ) and total pore volume ( $V_T$ , 1.3 vs. 0.4  $cm^3 g^{-1}$ ) compared to AC (Fig. 2e and Table S1). Both bio-AC and AC materials are enriched with microporous structures, both containing micropores of  $\sim 0.74$  nm and  $\sim 1.2$  nm in size, while bio-AC has an additional mesoporous structure ( $\sim 2$  nm). Furthermore, bio-AC had a trace amount of K element (2.4 wt% from ICP-OES, Table S2), which originated from the raw RH, as evidenced by XRF results (Table S3), whereas AC contained almost no K element ( $<0.1$  wt %). By comparing the catalytic deoxygenation performance of AC and K-doped AC, it was found that the K element contributed to the enhanced catalytic performance (Fig. 2f). Thus, the excellent catalytic activity of bio-AC towards the deoxygenation of stearic acid under  $H_2$ -free and solvent-free conditions is attributed to the oxygen-containing group and K element.

### 3.2. Characterization and catalytic activity of bio-AC-supported Ni catalysts

Previous studies have proven that inexpensive Ni-based catalysts (e.g., Ni/ZrO<sub>2</sub> and NiO/Al-SBA-15 catalysts) exhibited comparable activity to precious metals in the fatty acid catalytic deoxidation reaction [37, 49]. Herein, metallic Ni was loaded on carbonaceous supports (bio-AC and AC) to further enhance the catalytic deoxygenation activity. As illustrated in Fig. 3a–e, both TEM and EDX images revealed that there were two types of Ni particles dispersed on bio-AC support, that is nanoclusters (NCs, size of 1.1 nm) and nanoparticles (NPs, size of 13.6 nm). A similar result was found in Ni/AC catalyst (Fig. S5). Regarding the Ni loading amount, the ICP-OES result showed that the Ni loadings of the prepared Ni/bio-AC and Ni/AC catalysts were 6.2 wt% and 5.0 wt%, respectively.

The presence of crystalline Ni in both samples was confirmed by XRD characterization (Fig. S6). Raman spectra showed that the  $I_D/I_G$  values of both AC and bio-AC decreased upon loading of Ni (Fig. 4a), indicating that some Ni NCs or NPs were anchored to carbon defects caused by oxygen-containing groups [50,51]. As compared to bio-AC (1778 vs. 2670  $m^2 g^{-1}$ ) and AC (791 vs. 878  $m^2 g^{-1}$ ), the immobilization of Ni had greatly decreased the corresponding  $S_{BET}$  (Fig. S7). In particular, the

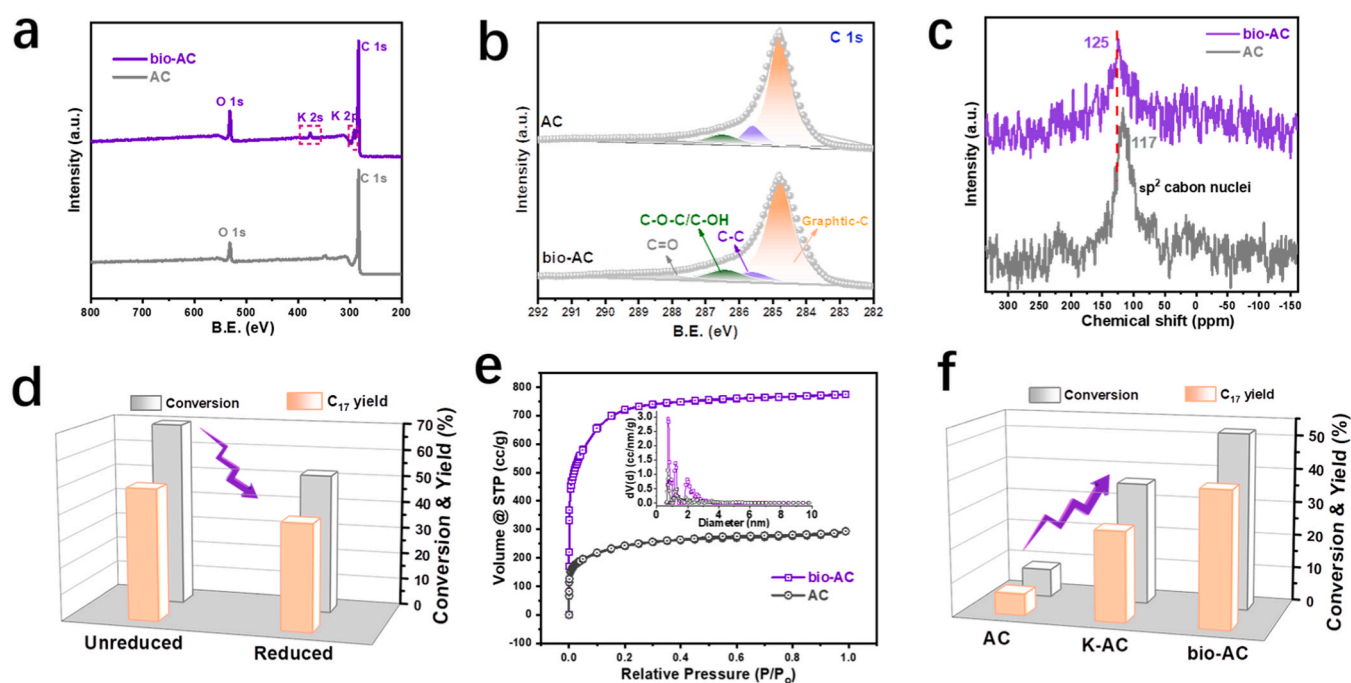


**Fig. 2.** (a) XPS survey scan spectra and (b) high-resolution C 1 s spectra of bio-AC and AC samples, (c)  $^{13}C$  MAS NMR spectra of bio-AC and AC samples, (d) catalytic performance of bio-AC before and after reduction, (e)  $N_2$  physisorption isotherms of bio-AC and AC samples, and the inset shows the corresponding pore size distribution plots, which were determined by the DFT model using the desorption data, and (f) catalytic performance of pure AC and K-doped AC catalysts.



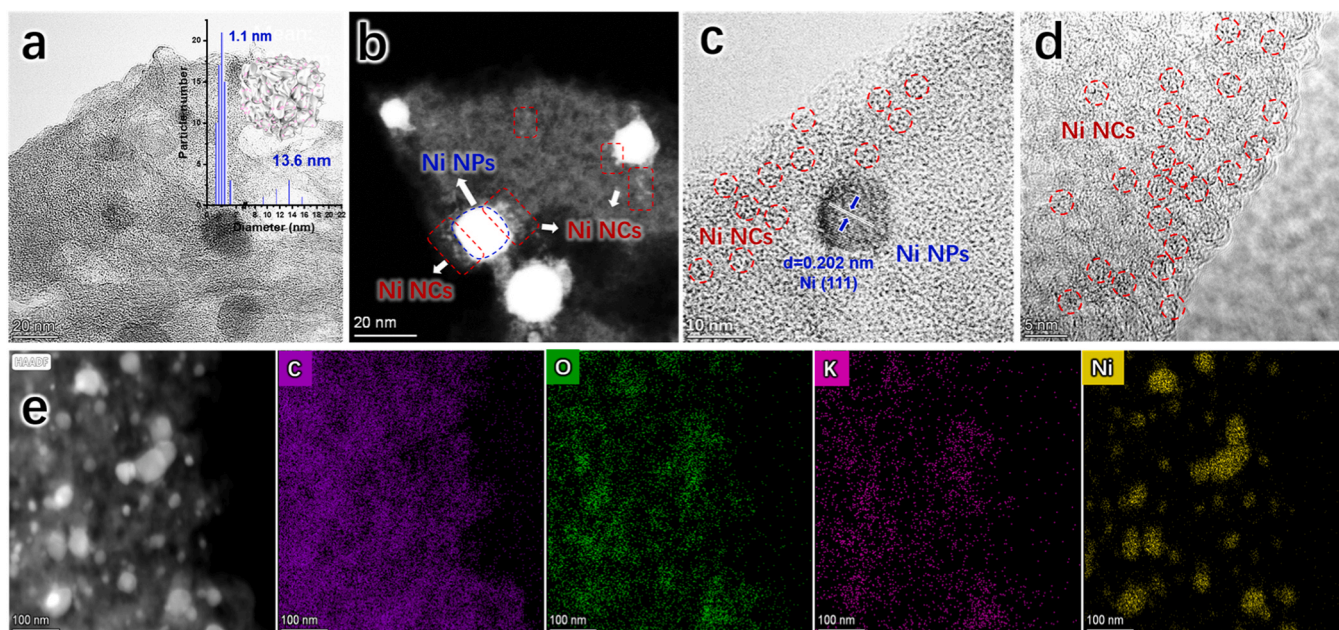


**Fig. 3.** (a-d) Representative TEM and scanning TEM images of Ni/bio-AC with corresponding size distribution histograms of Ni particles (inset), and (e) EDX elemental maps of Ni/bio-AC catalyst.

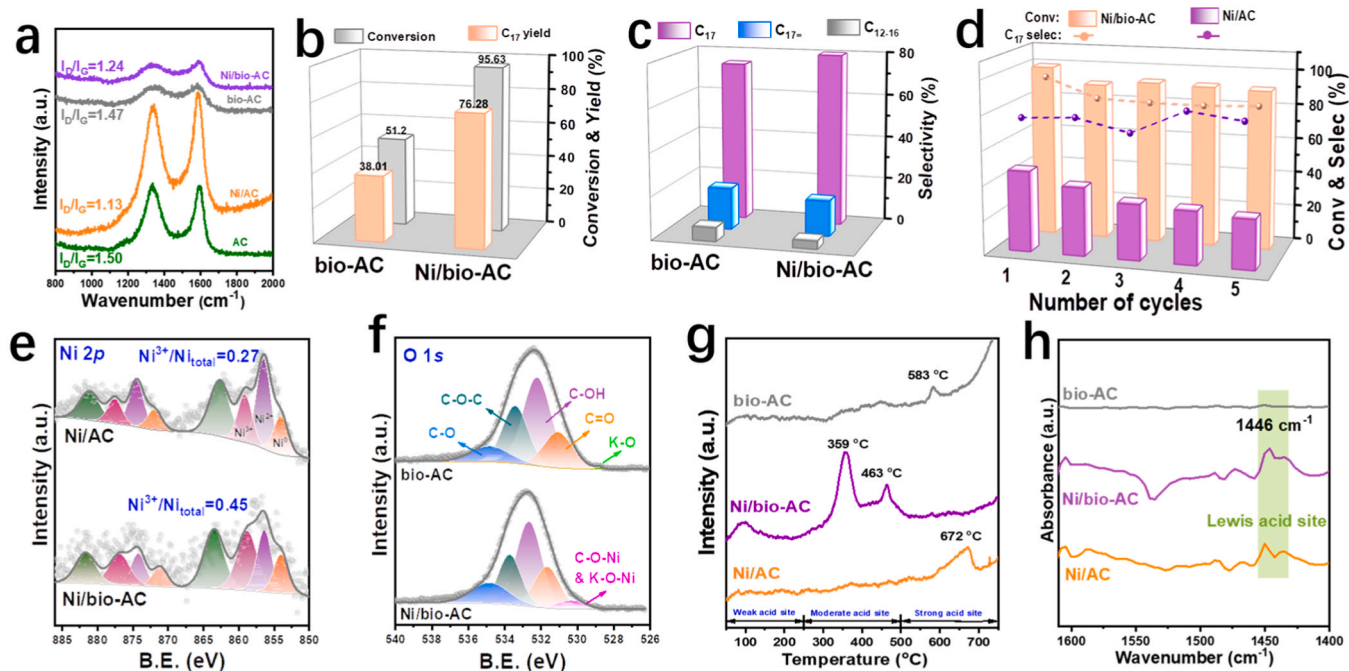


**Fig. 4.** Characterization and catalytic performance of bio-AC and Ni/bio-AC catalysts. (a) Raman spectra characterization, (b) catalytic performance in the  $H_2$ -free catalytic deoxygenation of stearic acid in a micro-batch reactor, (c) the corresponding product distribution, (d) cyclic stability test, (e) high-resolution XPS spectra in Ni 2p region, (f) high-resolution XPS spectra in O 1s region, (g)  $NH_3$ -TPD characterization, and (h) pyridine-adsorbed IR spectra characterization.

micropore volumes of bio-AC (1.07 vs. 0.56  $cm^3 g^{-1}$ ) and AC (0.32 vs. 0.28  $cm^3 g^{-1}$ ) showed a significant decrease upon immobilization of Ni (Table S1). The micropore volume of Ni/bio-AC was found to decrease by 47.7%, much higher than that of Ni/AC (12.5%), indicating that Ni/bio-AC may be enriched with more Ni NCs (size < 2 nm). Moreover, FTIR spectra (Fig. S8) revealed that the IR band of the  $\nu_{as}(COO)$  of Ni/bio-AC shifted significantly compared to that of bio-AC (1568 vs. 1619  $cm^{-1}$ ), which might be due to the interaction between Ni and oxygen-containing groups.

Interestingly, the catalytic conversion of stearic acid (95.6 vs. 51.2%)

and  $C_{17}$  yield (76.3 vs. 38.0%) over Ni/bio-AC were significantly higher as compared to that of bio-AC (Fig. 4b). Meanwhile, the  $C_{17}$  selectivity was also improved (79.8 vs. 74.2%, Fig. 4c). The catalytic performance of Ni/bio-AC was considerably better than that of Ni/AC with commercial AC support (Fig. S9a, b). This is especially true at a low reaction temperature (340 °C), whereby the  $C_{17}$  yield of Ni/bio-AC was 7.7 times than that of Ni/AC (67.7 vs. 8.8%), and the selectivity of the  $C_{17}$  product was also higher (78.8 vs. 58.7%). When the reaction temperature was increased to 380 °C, the conversion of Ni/bio-AC was as high as 99.6%, with  $C_{17}$  and total alkanes selectivities of 88.9% and 95.5%,

corresponding to yields of 88.5% and 95.1%, respectively. The corresponding turnover frequency based on the Ni amount (TOF<sub>Ni</sub>) value was 327.7 h<sup>-1</sup>, which was 3.85 times that of Ni/AC (85.4 h<sup>-1</sup>, Fig. S9c). The catalytic performance reported in the literature regarding the deoxygenation of fatty acids to alkanes was summarized in Table S4. It can be clearly seen that the prepared Ni/bio-AC exhibited excellent catalytic activity in the H<sub>2</sub>-free and solvent-free systems, which was superior to most of the reported catalysts. In addition, Ni/bio-AC exhibited stable catalytic activity in the five consecutive reaction cycles, indicating excellent cycling stability. However, the deoxygenation conversion of Ni/AC decreased from 46.7% to 28.7% after five reaction cycles (Fig. 4d). TEM images show no significant agglomeration of Ni on the used Ni/bio-AC and Ni/AC catalysts (Fig. S10a,b). The ICP-OES results show that the Ni content of the used Ni/bio-AC catalyst did not decrease significantly (6.07 vs. 6.24 wt%, Fig. S10c,d). In comparison, the Ni content of the used Ni/AC catalyst decreased from the initial 5.01 to 3.85 wt%, indicating that the Ni/bio-AC was more resistant to leaching with superior catalytic stability.

The remarkably different activities of Ni/bio-AC and Ni/AC catalysts might be caused by the different natures of Ni. Thus, the high-resolution XPS of Ni 2p spectra were analyzed, indicating that three Ni species were present, including Ni<sup>0</sup>, Ni<sup>2+</sup>, and Ni<sup>3+</sup> valence states (Fig. 4e) [52]. In addition, a strong satellite peak corresponding to the higher valence Ni species was also observed at a binding energy of ~863.4 eV. The presence of Ni<sup>3+</sup> might be associated with the formation of oxygen-ligated Ni NCs [53,54]. Specifically, the electron was transferred from Ni to the oxygen-containing group [55,56]. The ratio of Ni<sup>3+</sup>/Ni<sub>total</sub> in Ni/bio-AC was much higher than that of Ni/AC (45 vs. 27%), indicating a higher percentage of Ni NCs. Moreover, deconvolution analysis of both O 1s and C 1s XPS spectra revealed the presence of oxygen-containing groups (such as C-O, C-O-C, C-OH, C=O, and K-O) on bio-AC support (Fig. 4f and Fig. S11). Upon loading of Ni, the relative proportions of the C-OH group (44.7 vs. 40.6%) and C-O-C group (26.3 vs. 21.0%) decreased (see Fig. S12). A new peak at a binding energy of 530.2 eV may correspond to the metal-oxygen coordination site (C-O-Ni) [57]. Again, this indicates that oxygen-ligated Ni NCs are formed via the coordination of Ni to C-OH and C-O-C oxygen-containing groups (-OH-Ni-O-) [58].

In addition, previous studies have shown that the introduction of K<sup>+</sup> benefited the formation of Pt NCs upon hydrogen reduction, which owned a much smaller particle size than that of Pt without K<sup>+</sup> (0.9 vs. 4.5 nm) [59]. The XPS K 2p spectra were shifted upon Ni loading (Fig. S13), suggesting that there is an interaction between K species and Ni. The trace amount of K species (2.35 wt%) in bio-AC can also provide additional metal coordination sites to Ni in addition to the oxygen-containing groups, and the above-mentioned metal-to-metal interactions might promote the formation of more Ni NCs.

The acid site properties of the Ni/bio-AC catalyst were measured via NH<sub>3</sub>-TPD and Py-FTIR characterizations. The results demonstrated that Ni/bio-AC contains Lewis acid sites of moderate acidity (Fig. 4g, h), whereas bio-AC contains almost no acidic sites. It can be seen that the formation of Lewis acid sites is related to the Ni species [60]. The Lewis acid sites are active sites for fatty acid catalytic deoxygenation and the amount of moderate acids correlates positively with the rate of triglyceride conversion [12,61]. The stearic acid adsorption IR spectra demonstrated that Ni/bio-AC was more favorable for stearic acid adsorption and activation than Ni/AC (Fig. S14), which was similar to the DFT calculations by Liu et al. [53].

### 3.3. Characterization and catalytic activity of nitrogen-doped Ni/bio-AC

Although Ni/bio-AC catalyst showed excellent performance in the deoxygenation of stearic acid to paraffinic diesel hydrocarbons (total alkanes, 95.1% yield), the yield of the higher value-added long-chain olefins was low, which was only 4.5% at 380 °C. N-doping can alter the local charge distribution of the catalytic active site, thereby modulating its adsorption strength and conformation to the reactant/product and

improving the selectivity of the target product [62]. To enhance the production of long-chain olefins, nitrogen-doped Ni/bio-AC (denote Ni/bio-NAC) was prepared by using N-doped bio-AC as support to immobilize Ni (Fig. 5a) [63,64].

XPS survey (Fig. S15) and EDX elemental maps (Fig. S16a) of Ni/bio-NAC showed the successful doping of N element into the carbonaceous material. TEM images (Fig. S16b-d) reveal that both Ni NPs and Ni NCs were present in Ni/bio-NAC catalyst, but the particle size of Ni NPs becomes larger (~32.8 nm). The actual Ni loading content of Ni/bio-NAC catalyst was 14.8 wt% obtained from ICP-OES analysis. The reason might be due to the fact that N doping (4.5% from the XPS results) can significantly enhance the adsorption capacity of metal ions, leading to a higher metal loading efficiency. In addition, the higher loading content probably led to the large particle size (Table S2). The characteristic diffraction peaks for metallic Ni were also observed in the corresponding XRD curves (Fig. S17). Regarding the catalytic deoxygenation performance, compared to Ni/bio-AC, the yield of catalytic deoxygenation of stearic acid to C<sub>17=</sub> product over Ni/bio-NAC catalyst was significantly improved (18.7 vs. 4.5%). Also, compared to bio-NAC, Ni/bio-NAC showed higher conversion (38.0 vs. 21.6%, Fig. 5b), C<sub>17=</sub> selectivity (49.1 vs. 32.2%, Fig. 5c), and C<sub>17=</sub> yield (18.7 vs. 6.9%, Fig. 5b). Again, this suggests that the Ni species on bio-NAC contribute to the formation of value-added C<sub>17=</sub>. However, decreasing the Ni loading amount of Ni/bio-NAC catalyst did not significantly change the selectivity of C<sub>17=</sub> products (Fig. S18), suggesting that the improved olefin selectivity may be related to the interaction of Ni with N.

Furthermore, the XPS result indicates that the introduction of N was able to decrease the amount of C-OH group on the surface significantly through the amidation reaction (Fig. 5d). By comparing the catalytic performance of bio-AC and bio-NAC, N doping treatment was able to decrease the conversion (51.2 vs. 21.6%) and selectivity for C<sub>17</sub> products (76.4 vs. 56.0%). However, the selectivity for C<sub>17=</sub> was greatly improved (18.7 vs. 32.8%). In addition, for Ni/bio-NAC, the content of the metal-oxygen connection site (C-O-Ni) on oxygen-ligated Ni NCs was also decreased due to the reduction of C-OH anchor sites (Fig. S19). Therefore, it is deduced that the C-OH in oxygen-containing groups is the active site for the stearic acid catalytic deoxygenation to C<sub>17</sub>. Consequently, we also investigated the effect of N doping amount on the catalytic deoxygenation performance of Ni/bio-NAC catalysts. As can be seen in Fig. S20, the best catalytic performance of Ni/bio-NAC was achieved when the N doping amount was 0.03 mmol, with the highest C<sub>17=</sub> selectivity of 49.2%. Furthermore, the Ni/bio-NAC catalyst also exhibited good cycling stability with no significant decrease in conversion (38.8 vs. 34.9%) and C<sub>17=</sub> selectivity (49.2 vs. 49.9%) after five consecutive cycling reactions (Fig. S21). A slight improvement in the second cycle performance was attributed to dynamic changes in the catalyst surface during the reaction. The results of NH<sub>3</sub>-TPD and Py-FTIR analysis showed that Ni/bio-NAC did not have moderate Lewis acid sites but had strong Lewis acid sites (Fig. 5e, f), which is another reason for the reduced activity of C<sub>17</sub> product generation.

After loading Ni on bio-NAC support, a significant red-shift in the wavenumber of the corresponding C-N group was observed in the FTIR spectrum (1180 vs. 1103 cm<sup>-1</sup>, Fig. 5g), indicating the interaction of N with Ni (electron transfer from Ni to N), which led to the formation of the strong Lewis acid sites mentioned above. In addition, the Ni-N bond was also observed in the XPS spectra of N 1s (Fig. S22). This shows that in addition to the C-O-C mentioned above, Ni also coordinates with substituted C-N, resulting in the formation of N and O co-ligated Ni NCs containing strong Lewis acid sites. CO-TPD analysis revealed a higher CO desorption temperature upon the introduction of N (Fig. 5h), suggesting that the strong Lewis acidic sites on Ni/bio-NAC had enhanced the adsorption strength of carboxylic acid groups (-COO\*) on stearic acid [25]. The decrease in C<sub>17</sub> product generation activity was mainly attributed to (1) the introduction of N eliminates the partial C-OH group and the moderate Lewis acid sites, which are the main active sites for C<sub>17</sub> production; and (2) the strong interaction of Ni with N forms strong



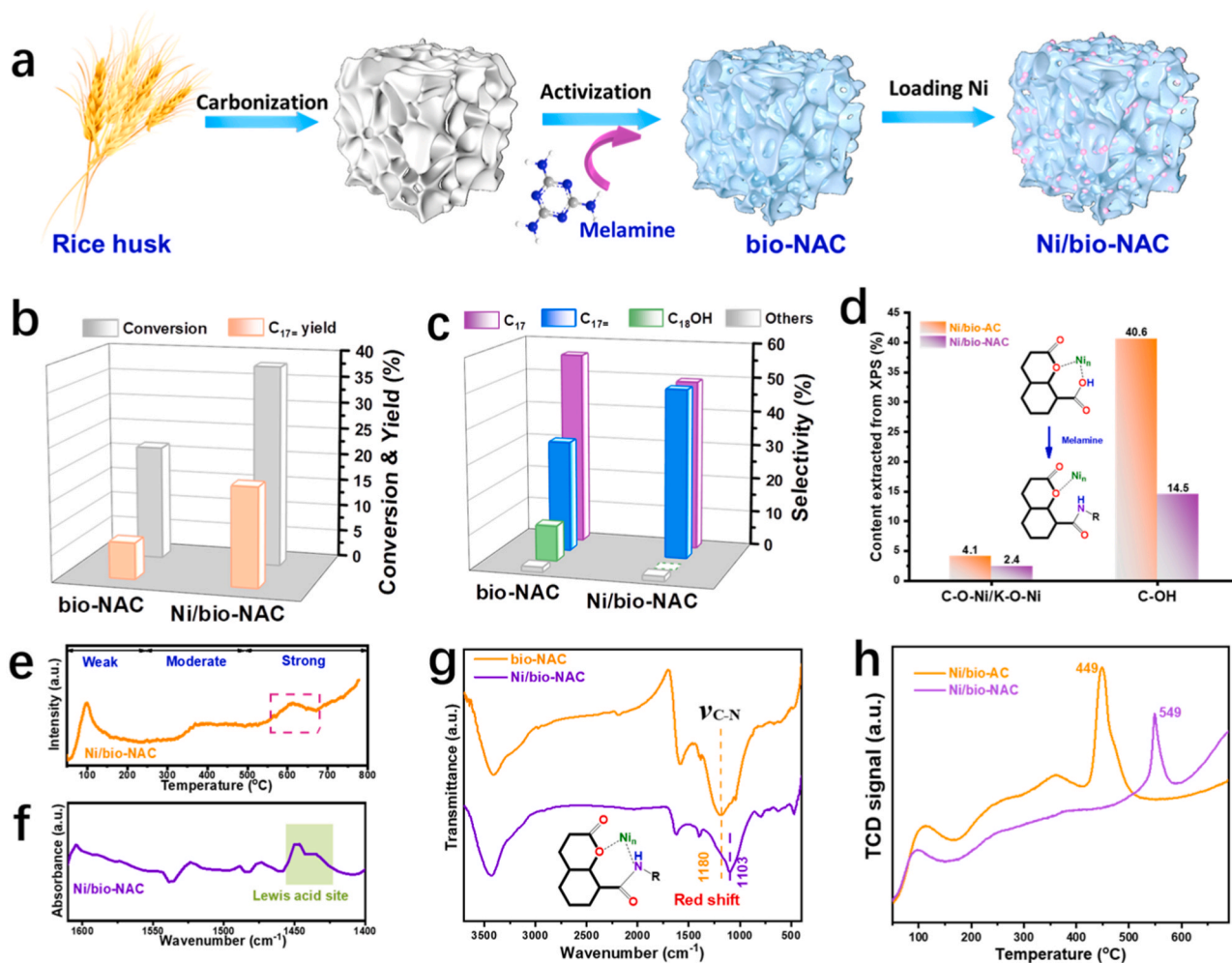


**Fig. 5.** (a) Schematic diagram of the preparation process of Ni/bio-NAC, (b) catalytic performance of bio-NAC and Ni/bio-NAC in the H<sub>2</sub>-free catalytic deoxygenation of stearic acid in a micro-batch reactor, and (c) the corresponding product distribution in different examples, (d) comparison of the partial oxygen-containing group content extracted from the XPS result of Ni/bio-AC and Ni/bio-NAC, (e) NH<sub>3</sub>-TPD profiles and (f) pyridine-adsorbed infrared spectra of Ni/bio-NAC, (g) FTIR spectra of bio-NAC and Ni/bio-NAC, and (h) CO-TPD profiles of Ni/bio-AC and Ni/bio-NAC.

Lewis acid sites whose strong adsorption for stearic acid inhibits the dissociation of -COO<sup>\*</sup>. The C<sub>17=</sub> product selectivity was enhanced as a result of the inhibition of C<sub>17</sub> production activity.

### 3.4. Reaction mechanism of the H<sub>2</sub>-free catalytic deoxygenation of stearic acid

In-situ DRIFTS were performed to investigate the catalytic deoxygenation reaction pathway under H<sub>2</sub>-free conditions (Fig. 6 and Fig. S23). As shown in Fig. 6a, for bio-AC, a redshift of the IR band due to the C=O group of stearic acid (1716 vs. 1702 cm<sup>-1</sup>) was observed, indicating that stearic acid was well-adsorbed on bio-AC. In addition, the increased band intensities of the stretching ( $\nu_{\text{CH}_3}$ ,  $\nu_{\text{CH}_2}$ ) and bending ( $\delta_{\text{CH}_3}$ ) vibrations of methyl and methylene groups are attributed to the formation of long-chain alkane products. A distinct band (2361 cm<sup>-1</sup>) ascribing to gas-phase CO<sub>2</sub> was also found, indicating that stearic acid was converted to long-chain alkanes (e.g., C<sub>17</sub>) mainly via decarboxylation reaction on bio-AC (Fig. 6b), where the oxygen-containing group (e.g., C-OH) is the major active site. Similarly, the above functional group changes were also found in the in-situ DRIFTS of Ni/bio-AC. Furthermore, upon Ni loading, a sharp -OH band corresponding to free water was first observed, followed by a broad -OH band corresponding to fatty alcohols (Fig. 6c), suggesting that the introduction of Ni promotes the in-situ dehydrogenation of stearic acid or vapor phase

reforming, and the resulting hydrogen species was able to convert stearic acid to octadecanol intermediates by hydrodehydrogenation [13,27, 65]. Moreover, the catalytic experiments with octadecanol (C<sub>18</sub>OH) as the reactant verified that C<sub>18</sub>OH was predominantly converted to C<sub>17</sub> products on Ni/bio-AC (Fig. S24a). This suggests that in addition to the decarboxylation pathway, stearic acid was able to be converted into the C<sub>17</sub> product over Ni/bio-AC catalyst via hydrodeoxygenation pathway with C<sub>18</sub>OH as the intermediate (Fig. 6d), where the oxygen-ligated Ni NCs is the active site of the pathway. In contrast, for Ni/AC catalysts enriched with more Ni NPs, strong characteristic bands corresponding to gas-phase CO<sub>2</sub> were observed in the in-situ DRIFTS (Fig. S23), while the band corresponding to C<sub>18</sub>OH was weak, indicating that the Ni NPs are the main active sites for the decarboxylation of fatty acids.

For Ni/bio-NAC, the C<sub>18</sub>OH reaction intermediate was also observed, which was further converted into the C<sub>17</sub> product over the catalyst as well (Fig. S24b). In contrast, the characteristic band of CO<sub>2</sub> gas generated by the decarboxylation reaction pathway was very weak (Fig. 6e), indicating that the N doping could largely inhibit the decarboxylation pathway. It suggests that the C<sub>17</sub> product was mainly generated through the hydrodeoxygenation pathway with C<sub>18</sub>OH as the intermediate (Fig. 6f), which was consistent with the results of the above analysis. The characteristic band corresponding to the C-H bending vibration ( $\gamma_{\text{CH}}$ ) in the C<sub>17=</sub> product was also observed, which was generated by the decarbonylation and subsequent dehydration of stearic acid (see GC-MS



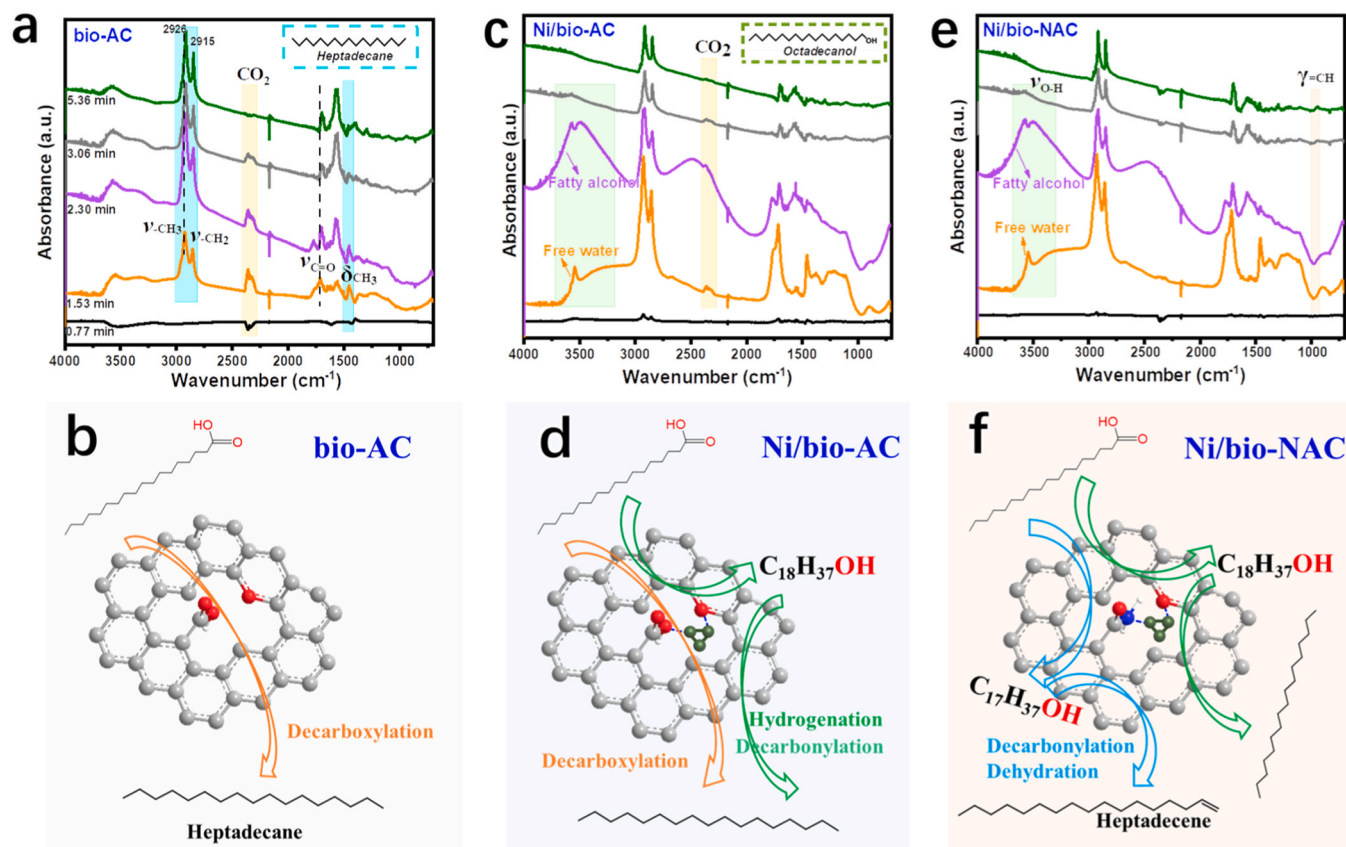


**Fig. 6.** In situ DRIFTS spectra and schematic diagrams of the corresponding catalytic reaction pathways of (a-b) bio-AC, (c-d) Ni/bio-AC, and (e-f) Ni/bio-NAC for  $H_2$ -free catalytic deoxygenation of stearic acid.

below). The detailed reaction pathway for the  $H_2$ -free catalytic deoxygenation of stearic acid over the catalysts is shown in Fig. 7.

### 3.5. Reaction performance of Ni/bio-NAC evaluated by Py-GC/MS

The high concentration of hydrogen species produced by fatty acid dehydrogenation or vapor phase reforming in the micro-batch reactor can lead to further hydrogenation of the  $C_{17=}$  product to  $C_{17}$ , consequently, lowering the olefin product selectivity. Recently, Py-GC/MS devices have been widely used for the qualitative and quantitative

analysis of catalytic pyrolysis products of plastics, rubber, and cellulose under flowing conditions wherein the dehydrogenation and aromatization reactions can occur in addition to deoxygenation reactions [66–68]. Accordingly, the Py-GC/MS device was also used to evaluate the catalytic pyrolysis performance of fatty acid over the Ni/bio-NAC catalyst under  $H_2$ -free conditions (referring to the detailed information of the device in Fig. S25).

In the absence of a catalyst, the conversion of stearic acid was extremely low (0.2%) and the products were oxygenated compounds (Fig. 8a, b). In comparison, 100% conversion was achieved at 405 °C

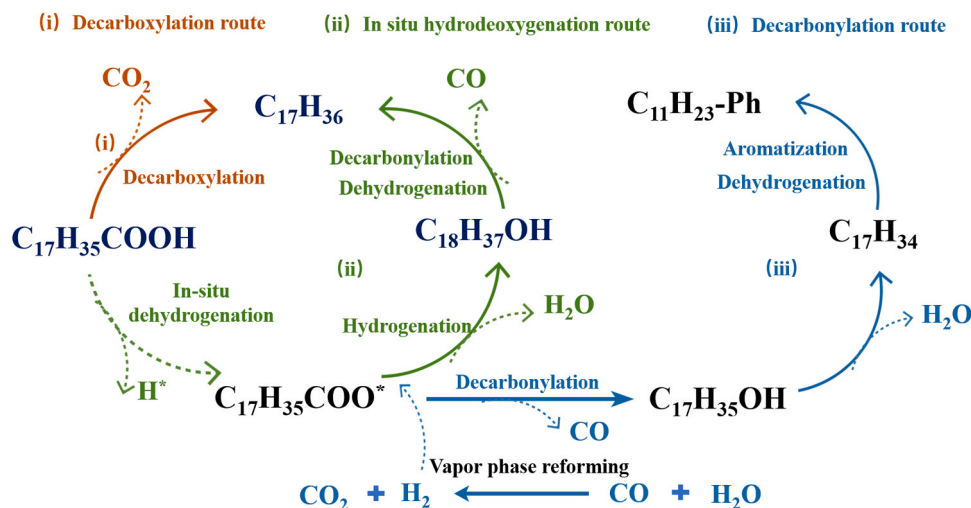


**Fig. 7.** Schematic diagram of the possible reaction pathways for hydrogen-free catalytic deoxygenation of stearic acid.

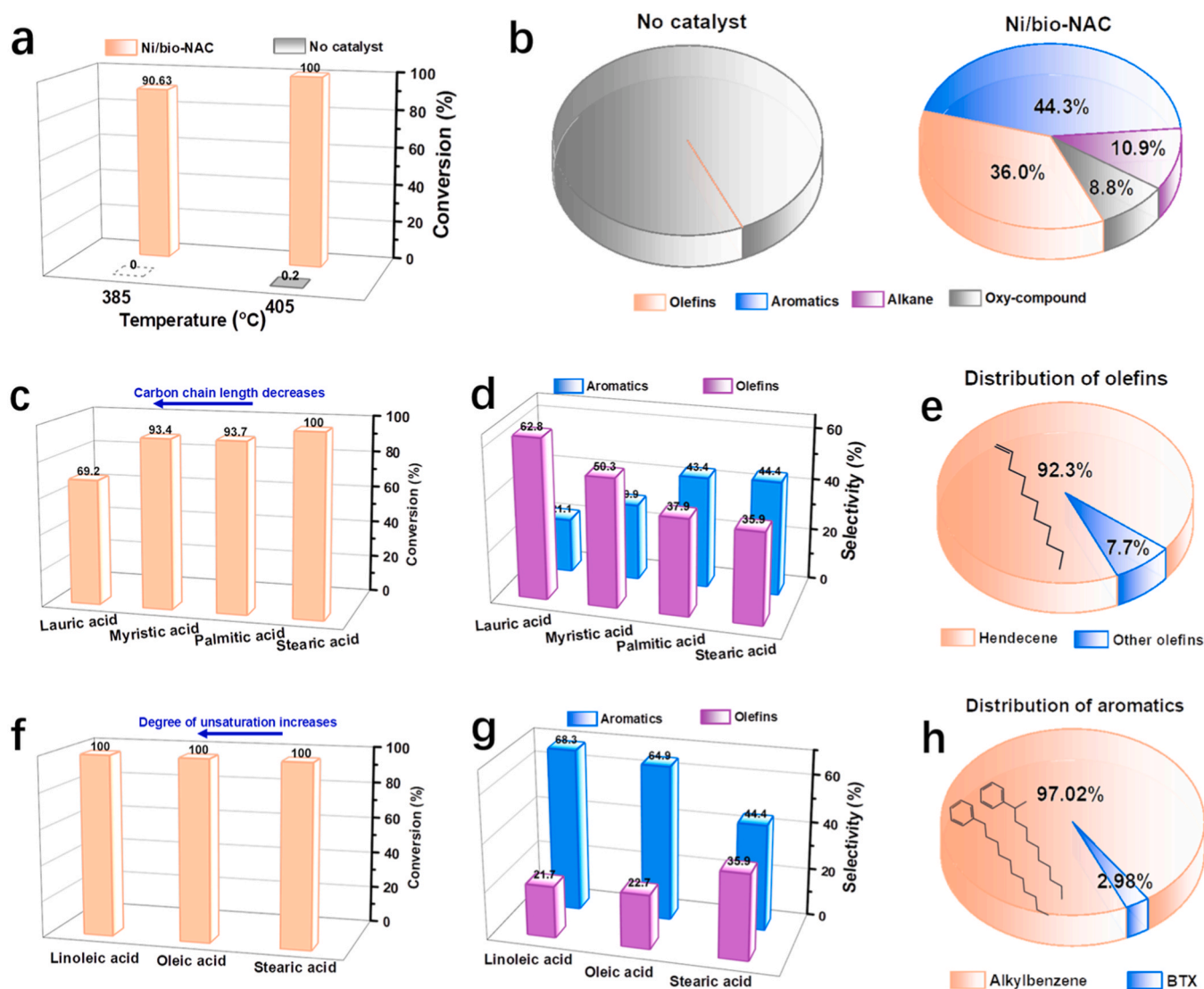


**Fig. 8.** (a) Conversion of stearic acid via the  $H_2$ -free pulsed catalytic pyrolysis process evaluated by Py-GC/MS device and (b) the corresponding reaction product distribution at the pyrolysis temperature of 405 °C, (c-e) catalytic performance towards fatty acids pyrolysis with different carbon chain lengths over Ni/bio-NAC catalysts, and (f-h) catalytic performance towards fatty acids pyrolysis with different degrees of unsaturation over Ni/bio-NAC catalysts.

with Ni/bio-NAC catalyst and the main products were olefins (36.0%) and aromatics (44.3%), and the selectivity for oxygenated compounds was less than 8.8%. Olefin products are usually obtained by fatty acid decarbonylation followed by dehydration or further pyrolysis, while the formation of the aromatic products should be complex with multiple reactions. Under low fatty acid concentration conditions (fatty acid/catalyst mass = 1/3), in-situ DRIFTS were used to explore the mechanism of the catalytic pyrolysis of stearic acid to aromatic products on Ni/bio-NAC. As shown in Fig. 9a, in-situ DRIFTS found a strong aliphatic alcohol characteristic band at  $3380\text{ cm}^{-1}$ , which gradually decreased with increasing reaction time, while the characteristic bands corresponding to aromatics ( $1606$ ,  $1560$ ,  $1506$ , and  $1460\text{ cm}^{-1}$ ) gradually increased. This suggests that aliphatic alcohol is a key intermediate for the formation of aromatic products. The GC-MS profiles of Ni/bio-NAC for stearic acid catalytic pyrolysis at 385 °C obtained on the Py-GC/MS device observed a large amount of heptadecanol product ( $C_{17}OH$ , 38.8%, Fig. 9b), while the conversion of  $C_{17}OH$  to  $C_{17}=$  and long-chain alkyl benzene was observed when the reaction temperature was increased to 405 °C (Fig. 9c). Using the  $C_{17}=$  as the reaction substrate, the conversion of the  $C_{17}=$  to long-chain alkylbenzene on Ni/bio-NAC was confirmed as detected by GC-MS analysis (Fig. 9d).

Taken together, under pulsed catalytic pyrolysis conditions, stearic acid is firstly transformed into the  $C_{17}OH$  intermediate over Ni/bio-NAC catalyst by decarbonylation, followed by dehydration to the  $C_{17}=$  product, which undergoes hydrogen transfer and aromatization at the strong Lewis acid site to form long-chain alkylbenzene. In contrast, the aromatization process was inhibited by the high concentration of hydrogen species generated by fatty acid dehydrogenation in the microbatch reactor, and thus almost no aromatic products were observed.

It is well known that the properties of the fatty acids (e.g., carbon chain length and degree of unsaturation) usually affect the conversion and pyrolysis product distribution. Catalytic performance evaluation by Py-GC/MS device showed that the shorter the carbon chain length of the fatty acids, the more difficult it is for the generated olefin products to undergo aromatization reactions and hence, the higher the selectivity for long-chain olefins (Fig. 8c-e and Fig. S26). When the carbon chain length of the fatty acid was 12 (that is, using lauric acid as reactant), the selectivity of long-chain olefins was as high as 62.8%, among which the selectivity of undecene ( $C_{11}=$ ) was as high as 92.3%. To the best of our knowledge, the catalytic performance is superior to that of the catalysts reported in the literature so far (Table S5).

In addition, using the higher degree of unsaturation of fatty acids as

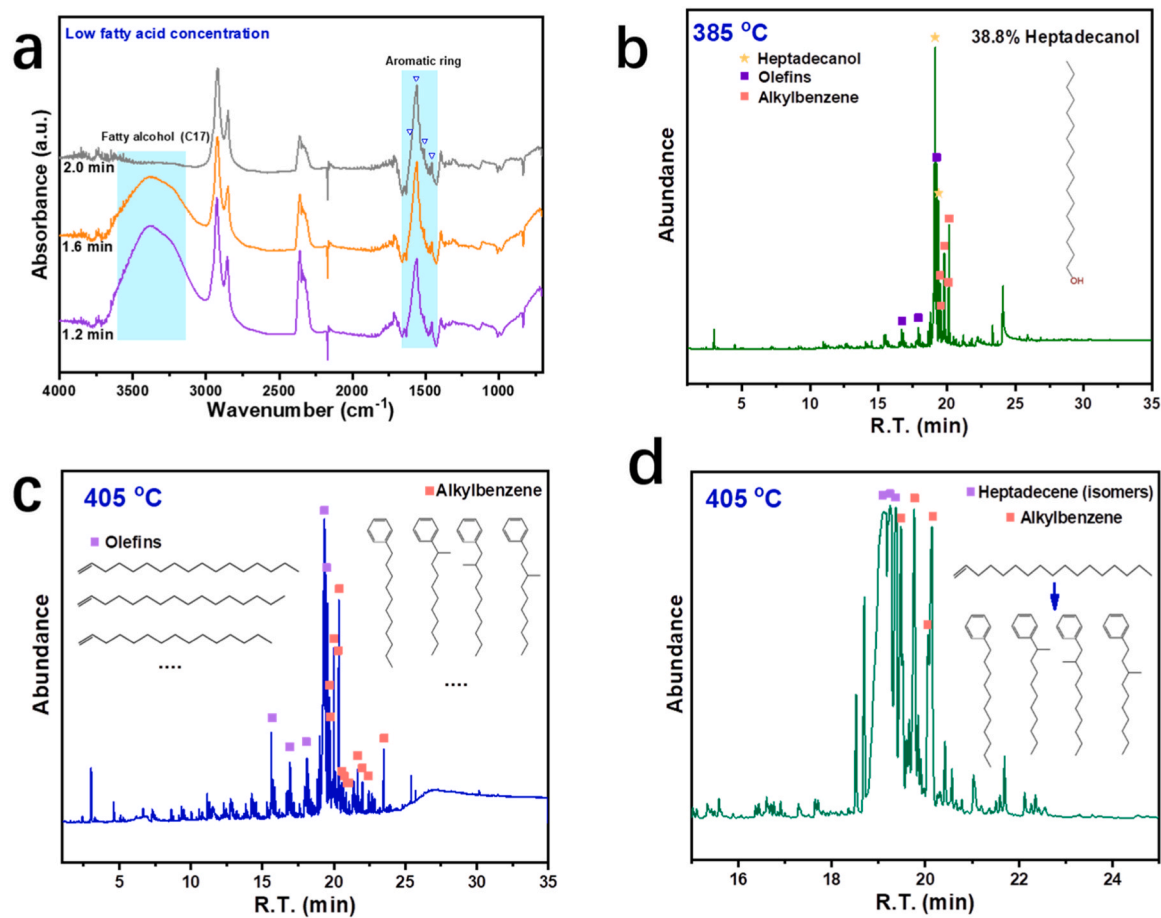


**Fig. 9.** (a) In situ DRIFTS for  $\text{H}_2$ -free catalytic pyrolysis of stearic acid over Ni/bio-NAC catalysts at low fatty acid concentrations (stearic acid/catalyst mass = 1/3). GC-MS profiles of  $\text{H}_2$ -free catalytic pyrolysis products of stearic acid over Ni/bio-NAC catalyst at (b) 385 °C and (c) 405 °C on the Py-GC/MS device, (d) GC-MS profile of the conversion products of heptadecene over Ni/bio-NAC catalyst at 405 °C on the Py-GC/MS device.

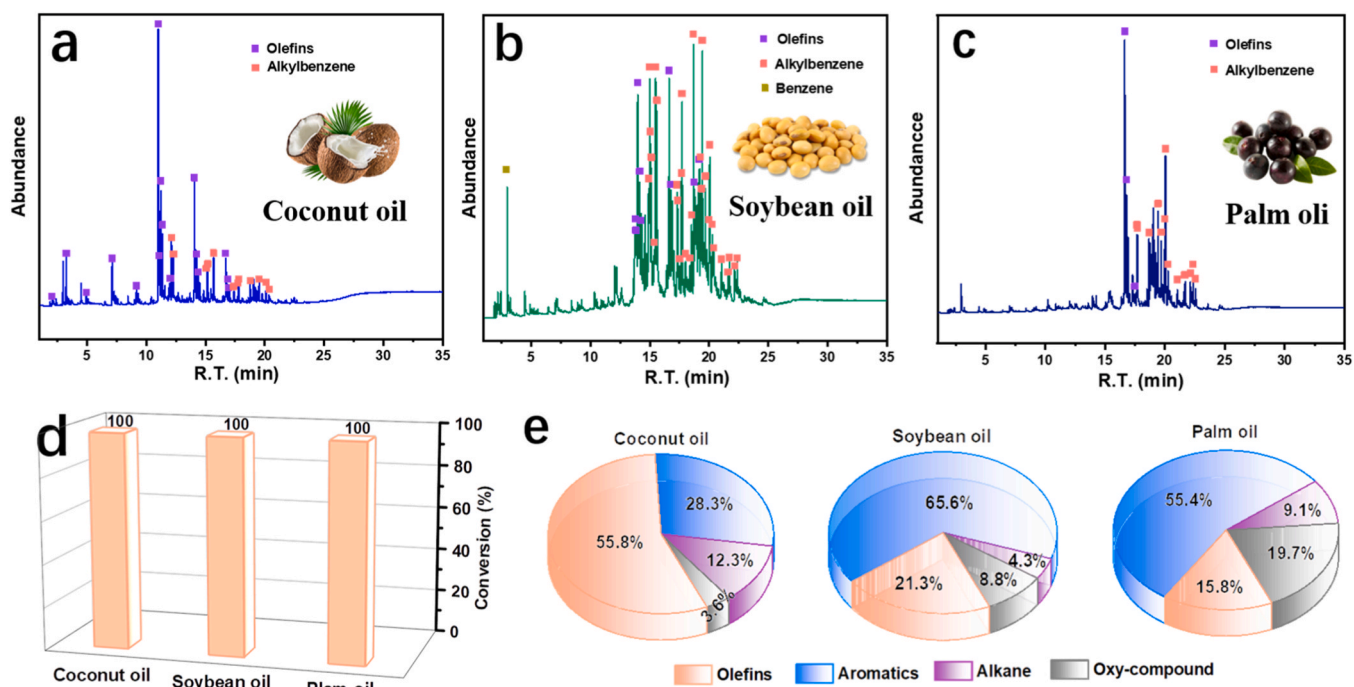


**Fig. 10.** GC-MS spectra of Ni/bio-NAC catalyst for pulsed catalytic pyrolysis of (a) coconut oil, (b) soybean oil, and (c) palm oil evaluated by Py-GC/MS device under  $\text{H}_2$ -free conditions, and the corresponding (d) conversions and (e) product distributions.



substrates, the olefin products are easy to undergo further aromatization (Fig. 8f-h and Fig. S27). When the degree of unsaturation of the aliphatic chains was 2 (linoleic acid as reactant), the aromatic selectivity was as high as 68.3%, with 97.1% for long-chain alkylbenzenes, which are important components for the production of surfactants, lubricants, refrigerants, and insulating oils, which are more valuable than long-chain alkanes. This provides a new pathway for the production of long-chain alkylbenzenes from the biomass-related source. Compared to the conventional BTX alkylation process, the above pathway is more environmentally friendly and sustainable (Fig. S28).

Furthermore, the Ni/bio-NAC catalyst also exhibited excellent performance for pyrolysis of wood-based oils such as coconut oil, soybean oil, and palm oil on the Py-GC/MS device, with conversions of up to 100% in all cases (Fig. 10a-d). Among them, the main products of the catalytic pyrolysis of coconut oil were long-chain olefins with a selectivity of 55.8% (Fig. 10e), while for soybean oil and palm oil, the main products were aromatic hydrocarbons with the selectivities of 65.6% and 55.4%, respectively. It can be seen that the prepared Ni/bio-NAC catalysts have good potential for producing bio-based chemicals such as long-chain olefins and alkylbenzenes.

#### 4. Conclusion

In summary, a series of Ni/bio-AC catalysts using the natural RH as the carbon source and biotemplate were fabricated and fully characterized, which exhibited excellent performance in the H<sub>2</sub>-free catalytic deoxygenation of stearic acid to biofuels (paraffinic diesel hydrocarbons), with yields up to 95.1% and the corresponding TOF value was 3.9 times that of the conventional Ni/AC catalyst. The high activity of the Ni/bio-AC catalyst was attributed to the synergistic effect of decarboxylation and hydrodeoxygenation active sites, with the abundant oxygen-containing groups (e.g., C-OH) and Ni NPs being the decarboxylation reactive sites, and the oxygen-ligated Ni NCs being the main hydrodeoxygenation reactive sites. It was found that the N doping on Ni/bio-NAC catalyst was able to further enhance the product selectivity for long-chain olefins in a micro-batch reactor, which was attributed to the elimination of decarboxylation and hydrodeoxygenation active sites and the interaction between Ni and N inhibiting -COO\* dissociation. The Ni/bio-NAC catalyst also showed excellent performance for the H<sub>2</sub>-free pulsed catalytic pyrolysis of fatty acids and oils (e.g., coconut oil, soybean oil, and palm oil) to bio-based chemicals such as long-chain olefins (optimum selectivity of 62.8%) and alkylbenzenes (optimum selectivity of 68.3%) under flow conditions evaluated on a Py-GC/MS device. Simultaneously, the effect of fatty acid properties (e.g., aliphatic chain length and degree of unsaturation) on the product distribution was investigated, which provided a valuable reference for the research of catalytic pyrolysis of plant oils to produce high-value chemicals.

#### CCRediT authorship contribution statement

**Bin Chen:** Conceptualization, Investigation, Writing – original draft. **Zining Zhou:** Methodology, Investigation. **Yuze Li:** Investigation. **Kok Bing Tan:** Writing – review & editing. **Youting Wang:** Investigation. **Xiaoping Rao:** Methodology. **Jiale Huang:** Conceptualization. **Xiaodong Zhang:** Conceptualization. **Qingbiao Li:** Methodology. **Guowu Zhan:** Writing – review & editing, Supervision, Conceptualization.

#### Declaration of Competing Interest

The authors declare that they have no known competing financial interests or personal relationships that could have appeared to influence the work reported in this paper.

#### Data Availability

Data will be made available on request.

#### Acknowledgments

This work was supported by the National Natural Science Foundation of China (Nos. U21A20324 and 22278167), and the Natural Science Foundation of Fujian Province (No. 2021J06026).

#### Appendix A. Supporting information

Supplementary data associated with this article can be found in the online version at doi:10.1016/j.apcatb.2023.123067.

#### References

- [1] A. Michaelowa, M. Allen, F. Sha, Policy instruments for limiting global temperature rise to 1.5°C – can humanity rise to the challenge? *Clim. Policy* 18 (2018) 275–286.
- [2] T.-H. D  ng, B.-H. Chen, D.-J. Lee, Optimization of biodiesel production from transesterification of triolein using zeolite LTA catalysts synthesized from kaolin clay, *J. Taiwan Inst. Chem. E* 79 (2017) 14–22.
- [3] P. Singh, Varun, S.R. Chauhan, Carbonyl and aromatic hydrocarbon emissions from diesel engine exhaust using different feedstock: a review, *Renew. Sust. Energ. Rev.* 63 (2016) 269–291.
- [4] I. Kubi  kov  , D. Kubi   ka, Utilization of triglycerides and related feedstocks for production of clean hydrocarbon fuels and petrochemicals: a review, *Waste Biomass Valor.* 1 (2010) 293–308.
- [5] Y. Wang, S. Ou, P. Liu, F. Xue, S. Tang, Comparison of two different processes to synthesize biodiesel by waste cooking oil, *J. Mol. Catal. A-Chem.* 252 (2006) 107–112.
- [6] Y. Luo, I. Ahmed, A. Kub  tov  , J.   t  v  , T. Aulich, S.M. Sadrameli, W.S. Seames, The thermal cracking of soybean/canola oils and their methyl esters, *Fuel Process. Technol.* 91 (2010) 613–617.
- [7] F.A.A. Twaig, A.R. Mohamad, S. Bhatia, Performance of composite catalysts in palm oil cracking for the production of liquid fuels and chemicals, *Fuel Process. Technol.* 85 (2004) 1283–1300.
- [8] A.W. Schwab, G.J. Dykstra, E. Selke, S.C. Sorenson, E.H. Pryde, Diesel fuel from thermal decomposition of soybean oil, *J. Am. Oil Chem. Soc.* 65 (1988) 1781–1786.
- [9] K.W. Cheah, S. Yusup, A.C.M. Loy, B.S. How, V. Skoulou, M.J. Taylor, Recent advances in the catalytic deoxygenation of plant oils and prototypical fatty acid models compounds: catalysis, process, and kinetics, *Mol. Catal.* 523 (2022), 111469.
- [10] S.K. Kim, J.Y. Han, H.-S. Lee, T. Yum, Y. Kim, J. Kim, Production of renewable diesel via catalytic deoxygenation of natural triglycerides: Comprehensive understanding of reaction intermediates and hydrocarbons, *Appl. Energy* 116 (2014) 199–205.
- [11] C. Kordulis, K. Bourikas, M. Gousi, E. Kordouli, A. Lycourghiotis, Development of nickel based catalysts for the transformation of natural triglycerides and related compounds into green diesel: a critical review, *Appl. Catal. B* 181 (2016) 156–196.
- [12] S. Janampelli, S. Darbha, Selective deoxygenation of fatty acids to fuel-range hydrocarbons over Pt-MO<sub>x</sub>/ZrO<sub>2</sub> (M = Mo and W) catalysts, *Catal. Today* 375 (2021) 174–180.
- [13] K.W. Cheah, M.J. Taylor, A. Osatiashtiani, S.K. Beaumont, D.J. Nowakowski, S. Yusup, A.V. Bridgwater, G. Kyriakou, Monometallic and bimetallic catalysts based on Pd, Cu and Ni for hydrogen transfer deoxygenation of a prototypical fatty acid to diesel range hydrocarbons, *Catal. Today* 355 (2020) 882–892.
- [14] Z. Zhang, H. Chen, C. Wang, K. Chen, X. Lu, P. Ouyang, J. Fu, Efficient and stable Cu-Ni/ZrO<sub>2</sub> catalysts for in situ hydrogenation and deoxygenation of oleic acid into heptadecane using methanol as a hydrogen donor, *Fuel* 230 (2018) 211–217.
- [15] S.A.W. Hollak, R.W. Gosselink, D.S. van Es, J.H. Bitter, Comparison of tungsten and molybdenum carbide catalysts for the hydrodeoxygenation of oleic acid, *ACS Catal.* 3 (2013) 2837–2844.
- [16] J. Zhang, X. Huo, Y. Li, T.J. Strathmann, Catalytic hydrothermal decarboxylation and cracking of fatty acids and lipids over Ru/C, *ACS Sustain. Chem. Eng.* 7 (2019) 14400–14410.
- [17] C. Jia, C. Zhang, S. Xie, W. Zhang, Z. Wang, H. Lin, One-pot production of jet fuels from fatty acids and vegetable oils in biphasic tandem catalytic process, *Fuel* 302 (2021), 121060.
- [18] N.A. Grosso-Giordano, T.R. Eaton, Z. Bo, S. Yacob, C.-C. Yang, J.M. Notestein, Silica support modifications to enhance Pd-catalyzed deoxygenation of stearic acid, *Appl. Catal. B* 192 (2016) 93–100.
- [19] J.P. Ford, J.G. Immer, H.H. Lamb, Palladium catalysts for fatty acid deoxygenation: Influence of the support and fatty acid chain length on decarboxylation kinetics, *Top. Catal.* 55 (2012) 175–184.
- [20] S. Janampelli, S. Darbha, Selective and reusable Pt-WO<sub>x</sub>/Al<sub>2</sub>O<sub>3</sub> catalyst for deoxygenation of fatty acids and their esters to diesel-range hydrocarbons, *Catal. Today* 309 (2018) 219–226.
- [21] C. Wang, Z. Tian, L. Wang, R. Xu, Q. Liu, W. Qu, H. Ma, B. Wang, One-step hydrotreatment of vegetable oil to produce high quality diesel-range alkanes, *ChemSusChem* 5 (2012) 1974–1983.
- [22] J.A. Lopez-Ruiz, R.J. Davis, Decarbonylation of heptanoic acid over carbon-supported platinum nanoparticles, *Green. Chem.* 16 (2014) 683–694.
- [23] S. Mondal, R. Singuru, S. Chandra Shit, T. Hayashi, S. Irle, Y. Hijikata, J. Mondal, A. Bhaumik, Ruthenium nanoparticle-decorated porous organic network for direct

- hydrodeoxygenation of long-chain fatty acids to alkanes, *ACS Sustain. Chem. Eng.* 6 (2017) 1610–1619.
- [24] J. Zhang, Z. Gao, S. Wang, G. Wang, X. Gao, B. Zhang, S. Xing, S. Zhao, Y. Qin, Origin of synergistic effects in bicomponent cobalt oxide-platinum catalysts for selective hydrogenation reaction, *Nat. Commun.* 10 (2019) 4166.
- [25] Z. Zhang, J. Tian, Y. Lu, X. Gou, J. Li, W. Hu, W. Lin, R.S. Kim, J. Fu, Exceptional selectivity to olefins in the deoxygenation of fatty acids over an intermetallic platinum-zinc alloy, *Angew. Chem. Int. Ed.* 61 (2022), e202202017.
- [26] W. Li, Y. Gao, S. Yao, D. Ma, N. Yan, Effective deoxygenation of fatty acids over Ni (OAc)<sub>2</sub> in the absence of H<sub>2</sub> and solvent, *Green. Chem.* 17 (2015) 4198–4205.
- [27] J. Zhong, Q. Deng, T. Cai, X. Li, R. Gao, J. Wang, Z. Zeng, G. Dai, S. Deng, Graphitic carbon embedded FeNi nanoparticles for efficient deoxygenation of stearic acid without using hydrogen and solvent, *Fuel* 292 (2021), 120248.
- [28] H. Yang, Y. Zeng, Y. Zhou, X. Du, D. Li, C. Hu, One-step synthesis of highly active and stable Ni-ZrO<sub>2</sub> catalysts for the conversion of methyl laurate to alkanes, *J. Catal.* 413 (2022) 297–310.
- [29] A. Srifa, K. Faungnawakij, V. Itthibenchapong, S. Assabumrungrat, Roles of monometallic catalysts in hydrodeoxygenation of palm oil to green diesel, *Chem. Eng. J.* 278 (2015) 249–258.
- [30] D. Zeng, Y. Li, H. Ma, F. Cui, J. Zhang, CuO@NiO nanoparticles derived from metal-organic framework precursors for the deoxygenation of fatty acids, *ACS Sustain. Chem. Eng.* 9 (2021) 15612–15622.
- [31] V.A. Yakovlev, S.A. Khromova, O.V. Sherstyuk, V.O. Dundich, D.Y. Ermakov, V. M. Novopashina, M.Y. Lebedev, O. Bulavchenko, V.N. Parmon, Development of new catalytic systems for upgraded bio-fuels production from bio-crude-oil and biodiesel, *Catal. Today* 144 (2009) 362–366.
- [32] M. Safa Gamal, N. Asikin-Mijan, M. Arumugam, U. Rashid, Y.H. Taufiq-Yap, Solvent-free catalytic deoxygenation of palm fatty acid distillate over cobalt and manganese supported on activated carbon originating from waste coconut shell, *J. Anal. Appl. Pyrol.* 144 (2019), 104690.
- [33] R.W. Gosselink, D.R. Stellwagen, J.H. Bitter, Tungsten-based catalysts for selective deoxygenation, *Angew. Chem. - Int. Ed.* 52 (2013) 5089–5092.
- [34] X. Cao, J. Zhao, F. Long, P. Liu, X. Jiang, X. Zhang, J. Xu, J. Jiang, Efficient low-temperature hydrogenation of fatty acids to fatty alcohols and alkanes on a Ni-Re bimetallic catalyst: The crucial role of NiRe alloys, *Appl. Catal. B* 312 (2022), 121437.
- [35] A. Vonortas, N. Papayannakos, Comparative analysis of biodiesel versus green diesel, *WIREs, Energy Environ.* 3 (2014) 3–23.
- [36] S.A.W. Hollak, J.H. Bitter, Jv Haveren, K.Pd Jong, D.Sv Es, Selective deoxygenation of stearic acid via an anhydride pathway, *RSC Adv.* 2 (2012) 9387.
- [37] K.B. Baharudin, Y.H. Taufiq-Yap, J. Hunns, M. Isaacs, K. Wilson, D. Derawi, Mesoporous NiO/Al-SBA-15 catalysts for solvent-free deoxygenation of palm fatty acid distillate, *Microporous Mesoporous Mater.* 276 (2019) 13–22.
- [38] D. Han, W. Yin, D. Luo, H. He, S. Wang, S. Xia, Hydrodeoxygenation of aliphatic acid over NiFe intermetallic compounds: Insights into the mechanism via model compound study, *Fuel* 305 (2021), 121545.
- [39] M. Snåre, I. Kubicková, P. Mäki-Arvela, K. Eränen, D.Y. Murzin, Heterogeneous catalytic deoxygenation of stearic acid for production of biodiesel, *Ind. Eng. Chem. Res.* 45 (2006) 5708–5715.
- [40] E. Santillan-Jimenez, M. Crocker, Catalytic deoxygenation of fatty acids and their derivatives to hydrocarbon fuels via decarboxylation/decarbonylation, *J. Chem. Technol. Biot.* 87 (2012) 1041–1050.
- [41] P. Tian, G. Zhan, J. Tian, K.B. Tan, M. Guo, Y. Han, T. Fu, J. Huang, Q. Li, Direct CO<sub>2</sub> hydrogenation to light olefins over ZnZrO<sub>x</sub> mixed with hierarchically hollow SAPO-34 with rice husk as green silicon source and template, *Appl. Catal. B* 315 (2022), 121572.
- [42] W. Li, K. Wang, G. Zhan, J. Huang, Q. Li, Hydrogenation of CO<sub>2</sub> to dimethyl ether over tandem catalysts based on biotemplated hierarchical ZSM-5 and Pd/ZnO, *ACS Sustain. Chem. Eng.* 8 (2020) 14058–14070.
- [43] X. Xu, Z. Li, R. Tu, Y. Sun, E. Jiang, Hydrogen from rice husk pyrolysis volatiles via non-noble Ni-Fe catalysts supported on five differently treated rice husk pyrolysis carbon supports, *ACS Sustain. Chem. Eng.* 6 (2018) 8325–8339.
- [44] T. Haynes, O. Ersen, V. Dubois, D. Desmecht, K. Nakagawa, S. Hermans, Protecting a Pd/CB catalyst by a mesoporous silica layer, *Appl. Catal. B* 241 (2019) 196–204.
- [45] J. Zhang, B. Xin, C. Shan, W. Zhang, D.D. Dionysiou, B. Pan, Roles of oxygen-containing functional groups of O-doped g-C<sub>3</sub>N<sub>4</sub> in catalytic ozonation: quantitative relationship and first-principles investigation, *Appl. Catal. B* 292 (2021), 120155.
- [46] X. Huang, W. Chu, W. Sun, C. Jiang, Y. Feng, Y. Xue, Investigation of oxygen-containing group promotion effect on CO<sub>2</sub>-coal interaction by density functional theory, *Appl. Surf. Sci.* 299 (2014) 162–169.
- [47] F. Yang, X. Ma, W.B. Cai, P. Song, W. Xu, Nature of oxygen-containing groups on carbon for high-efficiency electrocatalytic CO<sub>2</sub> reduction reaction, *J. Am. Chem. Soc.* 141 (2019) 20451–20459.
- [48] Z. Lu, G. Chen, S. Siahrostami, Z. Chen, K. Liu, J. Xie, L. Liao, T. Wu, D. Lin, Y. Liu, T.F. Jaramillo, J.K. Nørskov, Y. Cui, High-efficiency oxygen reduction to hydrogen peroxide catalysed by oxidized carbon materials, *Nat. Catal.* 1 (2018) 156–162.
- [49] B. Peng, X. Yuan, C. Zhao, J.A. Lercher, Stabilizing catalytic pathways via redundancy: selective reduction of microalgae oil to alkanes, *J. Am. Chem. Soc.* 134 (2012) 9400–9405.
- [50] Y. Ding, Z.A. Qiao, Carbon surface chemistry: new insight into the old story, *Adv. Mater.* 34 (2022), e2206025.
- [51] X. Bao, Y. Gong, Y. Chen, H. Zhang, Z. Wang, S. Mao, L. Xie, Z. Jiang, Y. Wang, Carbon vacancy defect-activated Pt cluster for hydrogen generation, *J. Mater. Chem. A* 7 (2019) 15364–15370.
- [52] K. Wan, J. Luo, C. Zhou, T. Zhang, J. Arbiol, X. Lu, B.W. Mao, X. Zhang, J. Fransaer, Hierarchical porous Ni<sub>3</sub>S<sub>4</sub> with enriched high-valence Ni sites as a robust electrocatalyst for efficient oxygen evolution reaction, *Adv. Funct. Mater.* 29 (2019), 1900315.
- [53] Y. Liu, J. Dai, N. Liu, Y. Wu, J. Huang, Y. Zheng, Q. Li, Oxygen-enriched biomass-activated carbon supported platinum nanoparticles as an efficient and durable catalyst for oxidation in benzene, *ACS Sustain. Chem. Eng.* 9 (2021) 7255–7266.
- [54] J.H. Kim, Y. Yuk, H.S. Joo, J.Y. Cheon, H.S. Choi, S.H. Joo, J.Y. Park, Nanoscale adhesion between Pt nanoparticles and carbon support and its influence on the durability of fuel cells, *Curr. Appl. Phys.* 15 (2015) S108–S114.
- [55] Y.-C. Zhang, C. Han, J. Gao, J. Wu, X.-D. Zhu, J.-J. Zou, Co<sub>3-x</sub>O<sub>4</sub>/NiO with abundant Ni<sup>3+</sup> active sites for boosting oxygen evolution reaction, *Chem. Eng. J.* 446 (2022), 137036.
- [56] Q. Yang, W. Xu, S. Gong, G. Zheng, Z. Tian, Y. Wen, L. Peng, L. Zhang, Z. Lu, L. Chen, Atomically dispersed Lewis acid sites boost 2-electron oxygen reduction activity of carbon-based catalysts, *Nat. Commun.* 11 (2020) 5478.
- [57] J.P. Ji, Y.P. Hou, S.Y. Zhou, T. Qiu, L. Zhang, L. Ma, C. Qian, S.D. Zhou, C.D. Liang, M. Ling, Oxygen-coordinated low-nucleus cluster catalysts for enhanced electrocatalytic water oxidation, *Carbon Energy* (2022) 1–11.
- [58] U.K. Thakur, P. Kumar, S. Gusarov, A.E. Kobryn, S. Riddell, A. Goswami, K. M. Alam, S. Savelle, P. Kar, T. Thundat, A. Meldrum, K. Shankar, Consistently high V<sub>oc</sub> values in p-n type perovskite solar cells using Ni<sup>3+</sup>-doped NiO nanomesh as the hole transporting layer, *ACS Appl. Mater. Interfaces* 12 (2020) 11467–11478.
- [59] L. Liu, M. Lopez-Haro, C.W. Lopes, C. Li, P. Concepcion, L. Simonelli, J.J. Calvino, A. Corma, Regioselective generation and reactivity control of subnanometric platinum clusters in zeolites for high-temperature catalysis, *Nat. Mater.* 18 (2019) 866–873.
- [60] P. Kumar, S.R. Yenumala, S.K. Maity, D. Shee, Kinetics of hydrodeoxygenation of stearic acid using supported nickel catalysts: effects of supports, *Appl. Catal. A* 471 (2014) 28–38.
- [61] M.-Y. Choo, J.C. Juan, L.E. Oi, T.C. Ling, E.-P. Ng, A. Rahman Noorsaadah, G. Centi, K.T. Lee, The role of nanosized zeolite Y in the H<sub>2</sub>-free catalytic deoxygenation of triolein, *Catal. Sci. Technol.* 9 (2019) 772–782.
- [62] A. Zhang, Y. Liang, H. Zhang, Z. Geng, J. Zeng, Doping regulation in transition metal compounds for electrocatalysis, *Chem. Soc. Rev.* 50 (2021) 9817–9844.
- [63] S. Liang, Q. Jiang, Q. Wang, Y. Liu, Revealing the real role of nickel decorated nitrogen-doped carbon catalysts for electrochemical reduction of CO<sub>2</sub> to CO, *Adv. Energy Mater.* 11 (2021), 2101477.
- [64] Z. Zhuang, S.A. Giles, J. Zheng, G.R. Jenness, S. Caratzoulas, D.G. Vlachos, Y. Yan, Nickel supported on nitrogen-doped carbon nanotubes as hydrogen oxidation reaction catalyst in alkaline electrolyte, *Nat. Commun.* 7 (2016) 10141.
- [65] N. Krobkrong, V. Itthibenchapong, P. Khongpracha, K. Faungnawakij, Deoxygenation of oleic acid under an inert atmosphere using molybdenum oxide-based catalysts, *Energ. Convers. Manag.* 167 (2018) 1–8.
- [66] J. Wang, J. Jiang, X. Wang, P. Liu, J. Li, G. Liu, K. Wang, M. Li, Z. Zhong, J. Xu, A. J. Ragauskas, Catalytic conversion of rubber wastes to produce aromatic hydrocarbons over USY zeolites: Effect of SiO<sub>2</sub>/Al<sub>2</sub>O<sub>3</sub> mole ratio, *Energ. Convers. Manag.* 197 (2019), 111857.
- [67] J. Wang, J.C. Jiang, D.X. Li, X.Z. Meng, G.W. Zhan, Y.P. Wang, A.H. Zhang, Y. J. Sun, R.G. Ruan, A.J. Ragauskas, Creating values from wastes: Producing biofuels from waste cooking oil via a tandem vapor-phase hydrotreating process, *Appl. Energy* 323 (2022), 119629.
- [68] J. Wang, J. Jiang, Y. Sun, X. Meng, X. Wang, R. Ruan, A.J. Ragauskas, D.C. W. Tsang, Heterogeneous Diels-Alder tandem catalysis for converting cellulose and polyethylene into BTX, *J. Hazard Mater.* 414 (2021), 125418.